Eur. Phys. J. A **21**, 323–333 (2004)
DOI 10.1140/epja/i2003-10216-x

THE EUROPEAN
PHYSICAL JOURNAL A

Helicity dependence of the γp $\rightarrow$ Nπ channels and multipole analysis in the Δ region

The GDH and A2 Collaborations

J. Ahrens[9], S. Altieri[15,16], J.R.M. Annand[6], G. Anton[3], H.-J. Arends[9,a], K. Aulenbacher[9], R. Beck[9], C. Bradtke[1], A. Braghieri[15], N. Degrande[4], N. d'Hose[5], D. Drechsel[9], H. Dutz[2], S. Goertz[1], P. Grabmayr[17], K. Hansen[8], J. Harmsen[1], D. von Harrach[9], S. Hasegawa[13], T. Hasegawa[11], E. Heid[9], K. Helbing[3], H. Holvoet[4], L. Van Hoorebeke[4], N. Horikawa[14], T. Iwata[13,b], O. Jahn[9], P. Jennewein[9], T. Kageya[14], B. Kiel[3], F. Klein[2], R. Kondratiev[12], K. Kossert[7], J. Krimmer[17], M. Lang[9], B. Lannoy[4], R. Leukel[9], V. Lisin[12], T. Matsuda[11], J.C. McGeorge[6], A. Meier[1], D. Menze[2], W. Meyer[1], T. Michel[3], J. Naumann[3], A. Panzeri[15,16], P. Pedroni[15], T. Pinelli[15,16], I. Preobrajenski[9,12], E. Radtke[1], E. Reichert[10], G. Reicherz[1], Ch. Rohlof[2], G. Rosner[6], D. Ryckbosch[4], M. Sauer[17], B. Schoch[2], M. Schumacher[7], B. Seitz[7,c], T. Speckner[3], N. Takabayashi[13], G. Tamas[9], A. Thomas[9], L. Tiator[9], R. van de Vyver[4], A. Wakai[14], W. Weihofen[7], F. Wissmann[7], F. Zapadtka[7], and G. Zeitler[3]

[1] Institut für Experimentalphysik, Ruhr-Universität Bochum, D-44801 Bochum, Germany
[2] Physikalisches Institut, Universität Bonn, D-53115 Bonn, Germany
[3] Physikalisches Institut, Universität Erlangen-Nürnberg, D-91058 Erlangen, Germany
[4] Subatomaire en Stralingsfysica, Universiteit Gent, B-9000 Gent, Belgium
[5] CEA Saclay, DSM/DAPNIA/SPhN, F-91191 Gif-sur-Yvette Cedex, France
[6] Department of Physics & Astronomy, University of Glasgow, Glasgow G12 8QQ, UK
[7] II. Physikalisches Institut, Universität Göttingen, D-37073 Göttingen, Germany
[8] Department of Physics, University of Lund, Lund, Sweden
[9] Institut für Kernphysik, Universität Mainz, D-55099 Mainz, Germany
[10] Institut für Physik, Universität Mainz, D-55099 Mainz, Germany
[11] Faculty of Engineering, Miyazaki University, Miyazaki, Japan
[12] INR, Academy of Science, Moscow, Russia
[13] Department of Physics, Nagoya University, Chikusa-ku, Nagoya, Japan
[14] CIRSE, Nagoya University, Chikusa-ku, Nagoya, Japan
[15] INFN, Sezione di Pavia, I-27100 Pavia, Italy
[16] Dipartimento di Fisica Nucleare e Teorica, Università di Pavia, I-27100 Pavia, Italy
[17] Physikalisches Institut, Universität Tübingen, D-72076 Tübingen, Germany

Received: 11 July 2003 / Revised version: 16 January 2004 /

Communicated by R. Milner

Abstract. A high-quality double-polarization data set for the helicity dependence of the total and differential cross-sections for both $\gamma p \rightarrow N\pi$ channels in the Δ region has been obtained in the framework of the GDH experiment. The experiment, performed at the Mainz microtron MAMI, used a 4π detection system, a circularly polarized photon beam, and a longitudinally polarized frozen-spin target. These data are included in the database to perform a multipole analysis to determine the properties of the $\Delta(1232)$-resonance. For the resonant $\Delta(1232)$ multipoles we find a very good agreement with previous analyses, while the nonresonant ones show significant deviations.

PACS. 13.60.Le Meson production – 14.20.Gk Baryon resonances with $S = 0$ – 25.20.Lj Photoproduction reactions

1 Introduction

Single-pion photoproduction is presently one of the main sources of our information on the structure of the nucleon. Various partial-wave analyses that have been pursued

---

[a] e-mail: `arends@kph.uni-mainz.de`

[b] *Present address*: Department of Physics, Yamagata University, Yamagata 990-8560, Japan.

[c] *Present address*: II. Physikalisches Institut, Universität Gießen, Gießen, Germany.

for over thirty years have offered the possibility to study the properties and the photon couplings to the nucleon resonances.

However, despite this long history and a large experimental effort, our understanding of this process is far from complete. Many predicted states are not sufficiently well established and many properties of the observed states (*e.g.* coupling constants, branching ratios, helicity amplitudes) are only poorly known. This is true in particular for resonances above Δ, where a substantial overlap among the different resonances occurs.

The availability of tagged-photon beams and the possibility to measure single-polarization observables have greatly increased the precision of this work during the last years, giving the possibility to access the smaller (and less known) electromagnetic multipoles through their interference with the leading terms. This has been clearly demonstrated in the Δ-resonance region, where the beam asymmetry of single-pion photoproduction has been measured with a high precision [1–3] in order to precisely determine the role of the electric quadrupole component of the proton wave function in the $N \rightarrow \Delta$ transition.

The recent technological developments in the polarized-beam and polarized-target techniques have also opened the possibility to access double-polarization observables which were unmeasured up to now. The first double-polarized data for single-pion photoproduction, obtained in the framework of the GDH experiment to check the Gerasimov-Drell-Hearn sum rule, were recently published by our Collaboration [4,5]. The multipole analysis made with our double-polarization $p\pi^0$ data in the D_{13} region produced a significant change in the values of the leading multipoles related to the excitation of this resonance [5].

As a further step in this study, we present in this paper our results on the helicity dependence for both $\gamma p \rightarrow N\pi$ channels in the Δ region. In this energy region, where several precise measurements, including those of single-polarization observables, have been carried out, the main multipoles should be well determined. Therefore, we cannot expect a similar impact of the new data as in the second resonance region. Our multipole analysis will rather represent a consistency check of our new double-polarization data and will serve as a basis to improve our knowledge of the less important multipoles, like E_{1+}, for which our data has a good sensitivity.

2 Experimental system

Since the experimental setup used for this measurement has already been described in detail in refs. [4,6], we will restrict the present discussion to the relevant features related to the present experiment.

2.1 The photon beam

This measurement was carried out at the tagged-photon facility of the MAMI accelerator in Mainz. Circularly polarized photons were produced by bremsstrahlung of longitudinally polarized electrons [7].

The photon energies were determined by the Glasgow tagging spectrometer which analyzes the momenta of the electrons that have radiated bremsstrahlung photons. This detector system is able to tag photons in the range from 50 to 800 MeV with a resolution of about 2 MeV [8]. The tagging efficiency was continuously monitored throughout the experiment by an e^+e^- detector placed downstream of the main hadron detector. The efficiency of this device was regularly calibrated at low beam intensity against a lead glass detector with an absolute systematic error of 2%.

The source of polarized electrons, based on the photoeffect on strained GaAs crystals, delivered routinely electrons with a degree of polarization of about 75%. The degree of polarization was continuously measured during the whole experiment by Møller scattering on a magnetized iron foil with a precision of 3% [9]. Both electrons were detected in coincidence in the tagging spectrometer. A dedicated trigger ensured that the sum of the electron energies matched the beam energy. In order to have a high degree of photon polarization over the full photon energy range from pion threshold to 800 MeV, two different energies of the primary electron beam (855 MeV and 525 MeV) were selected. The polarization direction was flipped randomly every 2 seconds to minimize systematics effects.

2.2 The target system

Longitudinally polarized protons were provided by a frozen-spin butanol (C_4H_9OH) target [10]. The system consisted of a horizontal dilution refrigerator and a superconducting polarization magnet, which was used in the polarization phase together with a microwave system for dynamical nuclear polarization (DNP). During the measurement the polarization was maintained in the "frozen-spin" mode at temperatures of about 50 mK by an internal superconducting coil integrated into the dilution refrigerator. At 2.5 T, maximum polarization values close to 90% were obtained for the protons with a typical relaxation time in the "frozen-spin" mode of about 200 hours. The holding field was homogeneous enough to allow for continuous NMR monitoring of the target polarization during the experiment with an absolute precision of 1.6%.

2.3 The hadron detector

The photon-induced reaction products were registered by means of a detector system covering almost the full solid angle. It was based on the large-acceptance detector DAPHNE [11] which was complemented by forward detectors to increase the solid-angle acceptance (see fig. 1) DAPHNE is a charged-particle detector with cylindrical symmetry that consists of 3 coaxial multi-wire proportional chambers with cathode readout, surrounded by 16 segments of a ΔE-E-ΔE plastic scintillator telescope and by a double scintillator-lead sandwich which allows the detection of neutral pions with a useful efficiency. Its

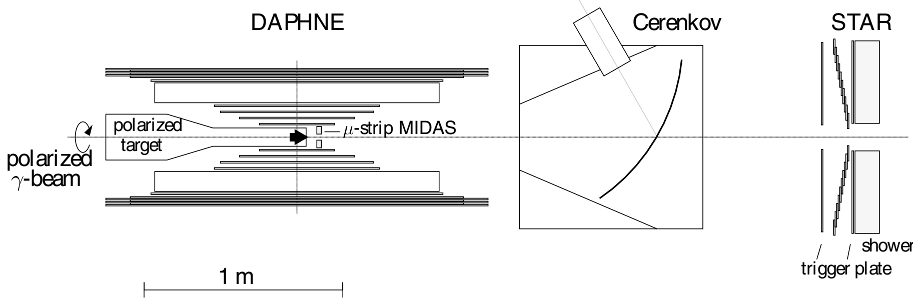

Fig. 1. Schematic side view of the GDH detector at MAMI.

most relevant characteristics are: i) high-precision measurement of the angles of emission of the charged particles ($\Delta\vartheta \leq 1°$ FWHM and $\Delta\varphi \simeq 2°$ FWHM), ii) good proton/π particle discrimination, iii) good proton momentum resolution ($\Delta p/p = 2.5$–10% for $p_p = 300$–900 MeV/c, iv) large solid-angle acceptance (polar acceptance $21° \leq \vartheta_{\mathrm{lab}} \leq 159°$ and full azimuthal acceptance), and v) large momentum acceptance (proton detection threshold: $p_p \simeq 260$ MeV/c, and charged pion detection threshold $p_\pi \simeq 70$ MeV/c for a 1 g/cm^2 target).

Three weaknesses are unfortunately inherent to the system. These are: i) no π^+/π^- discrimination, ii) no momentum measurement for those charged pions which do not stop in the detector and iii) no measurement of the angle of emission for neutral pions.

The compact silicon strip detector MIDAS [12], a charged-particle tracking telescope, covered the polar region from $\vartheta_{\mathrm{lab}} = 7°$ to $\vartheta_{\mathrm{lab}} = 16°$. The extreme forward angles were covered by the annular scintillator ring detector STAR [13] and a lead-scintillator sandwich counter, while an aerogel threshold Čerenkov detector served for online suppression of the electromagnetic background.

3 Data analysis

In this paper, only the data recorded by the DAPHNE detector will be presented.

Charged particles stopped inside the detector were identified using the range method described in [14], a maximum likelihood algorithm that uses simultaneously all the charged-particle energy losses in the DAPHNE scintillator layers to discriminate between protons and $\pi^\pm$ and determine their kinetic energies.

Since at least two energy loss samples along the charged track are needed, the domain of applicability of this method is restricted to particles that penetrate beyond the first scintillator layer. Protons stopped in the first scintillator layer were then identified by using a standard dE/dx-E technique, in which the wire chambers provide the dE/dx information and the first scintillator layer provides the E information [15].

The identification of the charged particles that have sufficient energy to escape the detector was performed by using the ΔE-E technique described in [16] which compares information provided by the geometrical path of the particle inside the detector with the energy deposited in the thickest scintillator layer.

3.1 The pπ^0 channel

The presence of a single charged track recognized as a proton was used as the signature for the $p\pi^0$ channel. Above $E\gamma \simeq 450$ MeV, where double-pion photoproduction processes cannot be neglected, the main background originates from the $p\pi^0\pi^0$ and $p\pi^+\pi^-$ channels. The separation between the single- and double-pion photoproduction channels was obtained from the analysis of the missing-mass spectrum $\gamma p \to pX$ [17]. The absolute efficiency of the $p\pi^0$ channel identification was evaluated using a GEANT-based simulation and was found to be between 85% and 95%.

Recoil protons from the $p\pi^0$ channel have enough energy to enter the DAPHNE detector only when $E_\gamma \geq 300$ MeV. In this case the kinematics is overdetermined and differential cross-sections can be given. Below $E_\gamma = 450$ MeV, when the proton does not escape the target, the π^0 is used as a signature for this channel. Since the π^0 angle cannot be measured by our apparatus, this information can only be used to evaluate the total cross-section for this channel.

The π^0 was identified by requiring a coincidence between the two photons resulting from its decay. For all π^0 energies and angles a fraction of these photons is detected inside our apparatus. Hence, no angular or momentum extrapolation was needed to evaluate the total photoabsorption cross-section for this channel below 450 MeV. The absolute π^0 detection efficiency varied between $\sim 15\%$ and $\sim 23\%$ and was evaluated using a GEANT-based simulation containing the full detector setup and with the complete set of geometrical and electronic thresholds taken into account.

A validation of the simulation was obtained by comparing the simulated efficiency for the $\gamma p \to p\pi^0$ channel with an efficiency measurement at photon energies where the recoil proton can be identified by the DAPHNE detector. Under this condition, ϵ_{π^0} is equal to the fraction of the events with a proton in the final state that have also two photons in coincidence. The result of this comparison is shown in fig. 2 where the two dashed lines represent the maximum and minimum efficiency values obtained from

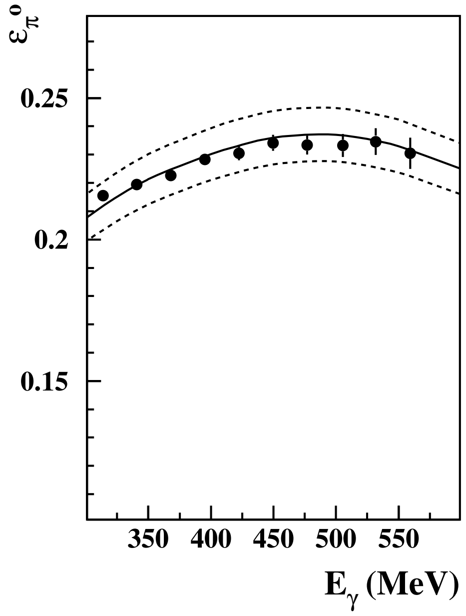

Fig. 2. Comparison between the simulated (solid line) and measured (solid circles) π^0 detection efficiency (ϵ_{π^0}) in the $\gamma p \to p\pi^0$ process as a function of photon energy. The dashed lines represent the estimated systematic error band of the simulation (±4% of ϵ_{π^0}).

the estimated systematic error of the simulation (4% of ϵ_{π^0}). The good agreement between simulation and experimental data gives confidence in the simulated efficiencies.

3.2 The $n\pi^+$ channel

The presence of a single charged track recognized as a pion was used as the signature for the $n\pi^+$ channel. Since DAPHNE is not used to detect neutrons alone, the minimum photon energy providing access to this channel with our setup is about 180 MeV, when π^+'s have enough energy to enter DAPHNE. For $E_\gamma > 300$ MeV, most of the π^+ escape the detector and their energy cannot be sufficiently well determined. The discrimination between the $n\pi^+$ and the $n\pi^+\pi^0$ channel is difficult. For this reason, the presented analysis is restricted to $E_\gamma \leq 450$ MeV, where the effects of double-pion processes are negligible.

In order to evaluate the total cross-section for this channel, an extrapolation is needed. For $E_\gamma > 200$ MeV, the region where the data of the total cross-section for this channel will be presented, the lower π^+ momentum limit is above the momentum threshold limit applied in the analysis and only an angular extrapolation is necessary. About 95% of the total cross-section is measured directly. The extrapolation into the unobserved region was made using the HDT calculation [18]. Since the total correction is of the order of 5% only, the estimated systematic error is assumed to be less than 2%.

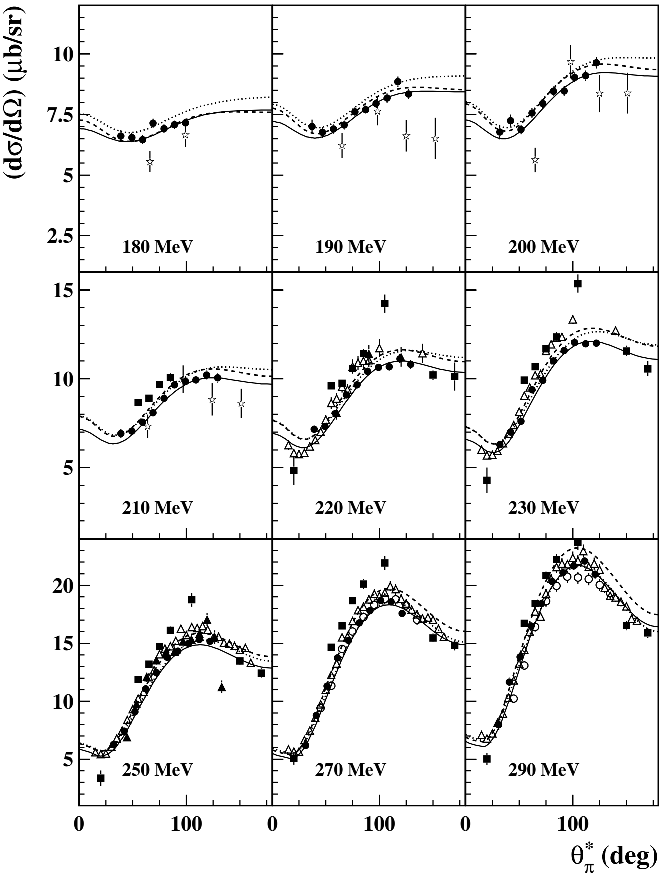

Fig. 3. The measured unpolarized differential cross-section for the $\gamma p \to n\pi^+$ reaction for photon energies from 180 to 290 MeV (solid circles) is compared to previous experimental data and to the SAID [19] (solid lines), MAID [20] (dashed lines) and HDT [18] (dotted lines) analyses. Open circles: [2]; open stars: [21]; open triangles: [22]; filled triangles: [23]; open squares: [24]; solid squares: [3]. The errors shown are statistical only.

3.3 Unpolarized differential cross-sections

Prior to the main experiment, data for detector energy calibration and for tests of the analysis methods were taken with the same apparatus using an unpolarized liquid-hydrogen target. The total unpolarized cross-sections for $\gamma p \to n\pi^+$ and $\gamma p \to p\pi^0$ in the Δ region were found to be in a good agreement [4] with previously published data and with predictions of multipole analyses.

Figures 3 and 4 show the unpolarized differential cross-sections for $\gamma p \to n\pi^+$ in the energy range $180\,\mathrm{MeV} < E_\gamma < 450\,\mathrm{MeV}$ [9] as a function of the pion center-of-mass (c.m.s.) angle ϑ^*_π. These data are compared to previous DAPHNE data [2], the data from Bonn [22–24] and Saskatoon [21], and to the results of the MAID [20], SAID [19], and HDT [18] theoretical analyses.

Similarly, in fig. 5 the unpolarized differential cross-sections for $\gamma p \to p\pi^0$ are shown in the energy range $310\,\mathrm{MeV} < E_\gamma < 540\,\mathrm{MeV}$ [9]. They are compared to the

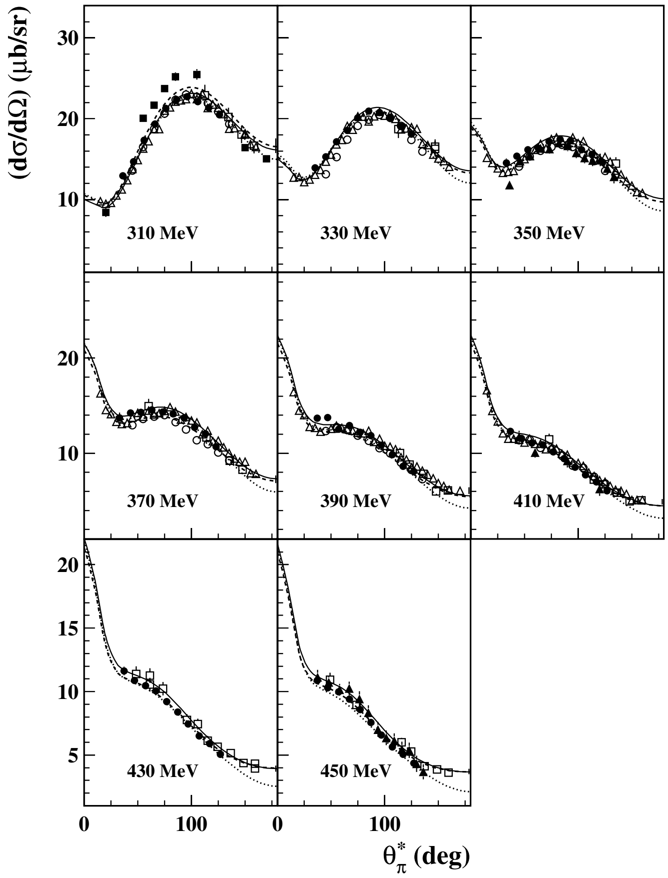

Fig. 4. As in fig. 3, but for photon energies from 310 to 450 MeV.

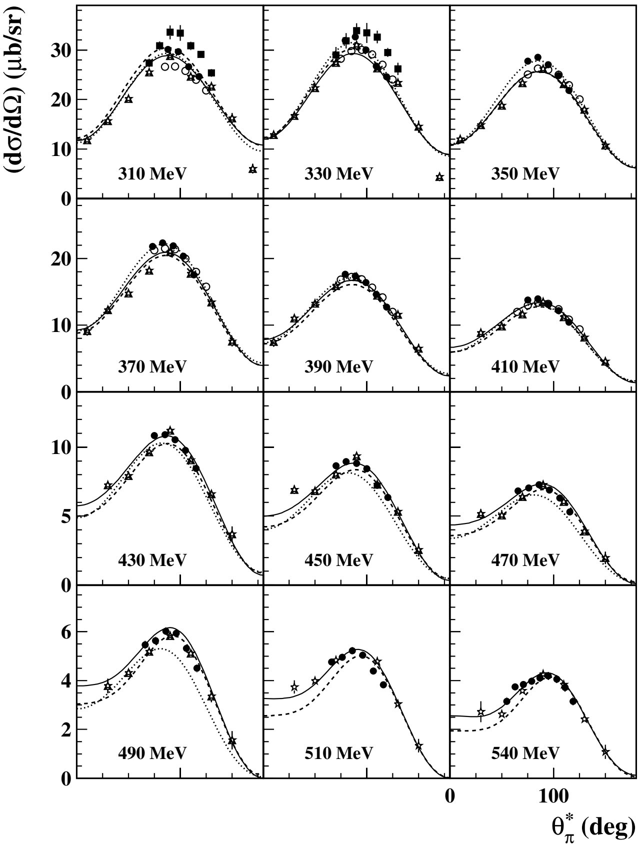

Fig. 5. The measured unpolarized differential cross-section for the $\gamma p \to p\pi^0$ reaction for photon energies from 310 to 540 MeV (solid circles) is compared to previous experimental data and to the model predictions. Curves as in figs. 3 and 4. Open circles: [1]; open stars: [25]; open triangles: [26]. The errors shown are statistical only.

same theoretical models as before, to previous DAPHNE data [1] and to the data of ref. [25] and ref. [22].

The agreement for both channels with the previous data and the models shows that the detector response is also well understood for the differential cross-section.

3.4 Polarized data

As previously discussed [4], in the analysis of data taken using the butanol target, the background contribution of the reactions on C and O nuclei could not be fully separated event by event from the polarized H contribution. However, this background from spinless nuclei is not polarization dependent and cancels when the difference between events in the 3/2 and 1/2 helicity states is taken [4], where 3/2 and 1/2 indicate the relative nucleon-photon spin configuration, parallel and antiparallel, respectively. For this reason, only the helicity-dependent total and differential cross-sections can be directly extracted from the measurement with the butanol target.

4 Experimental results

By using the methods described above, the helicity-dependent total cross-section $\sigma_{31} = (\sigma_{3/2} - \sigma_{1/2})$ was obtained in the photon energy range from photoproduction threshold to 450 MeV for the $p\pi^0$ channel and from 200 MeV to 450 MeV for the $n\pi^+$ channel. The obtained results are shown in fig. 6. These data contain the complete statistics of the collected data set and statistically improve the results shown in ref. [4]. In fig. 6, our data are also compared to the SAID [19] (solid curve), MAID [20] (dashed curve) and HDT [18] (dotted curve) analyses.

In figs. 7, 8 and 9 we present the obtained helicity-dependent differential cross-section $\Delta_{31} = (\mathrm{d}\sigma/\mathrm{d}\Omega)_{3/2} - (\mathrm{d}\sigma/\mathrm{d}\Omega)_{1/2}$ for the $n\pi^+$ channel (from 180 MeV up to 450 MeV) and for the $p\pi^0$ channel (from 310 MeV up to 540 MeV), respectively, and compare these data to the previously mentioned models. Data on Δ_{31} for the $p\pi^0$ channel at $E_\gamma > 550$ MeV have already been published [5] and were shown to be highly sensitive to the helicity amplitudes of the $D_{13}(1520)$-resonance.

All errors shown are statistical only. The systematic error contains contributions from charged-particle identification (2.5%), photon flux normalization (2%), photon polarization (3%), target polarization (1.6%), π^0 detection efficiency, and π^+ extrapolation. The addition of these

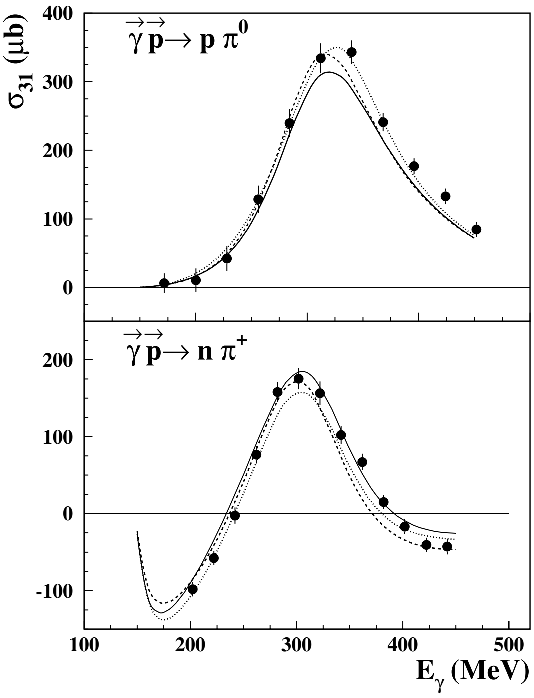

Fig. 6. The measured helicity-dependent total cross-section $\sigma_{31} = \sigma_{3/2} - \sigma_{1/2}$ for the $\vec{\gamma}\vec{p} \to p\pi^0$ (top) and $n\pi^+$ channels (bottom) is compared to the model predictions. Curves as in the previous figures. The errors shown are statistical only.

errors in quadrature leads to a total systematic error of about 6% for the $p\pi^0$ channel and of about 5% for the $n\pi^+$ channel.

Using the unpolarized cross-section data, it is also possible to evaluate separately the two helicity-dependent cross-sections $\sigma_{1/2}$ and $\sigma_{3/2}$. As an example, the resulting total cross-sections are shown in figs. 10 and 11 together with the model predictions.

In general, all the experimental cross-sections are reasonably well reproduced by the different analyses. However, small differences can be seen between models and data and among the models themselves. This is mainly due to the fact that the polarization observables show a higher sensitivity to the small electromagnetic multipoles than the unpolarized data. An example of such a sensitivity is shown in fig. 12 where our experimental results are compared to three different predictions of the HDT model in which the ratio between the (dominant) magnetic dipole ($M1$) and the (small) electric quadrupole radiation ($E2$) components of the proton → Δ transition has been varied. The data are well reproduced with an $E2/M1$ ratio of −2.5%.

In order to perform a meaningful determination of all the relevant electromagnetic multipoles in the photon energy range, a partial-wave analysis including these new data into the database was performed.

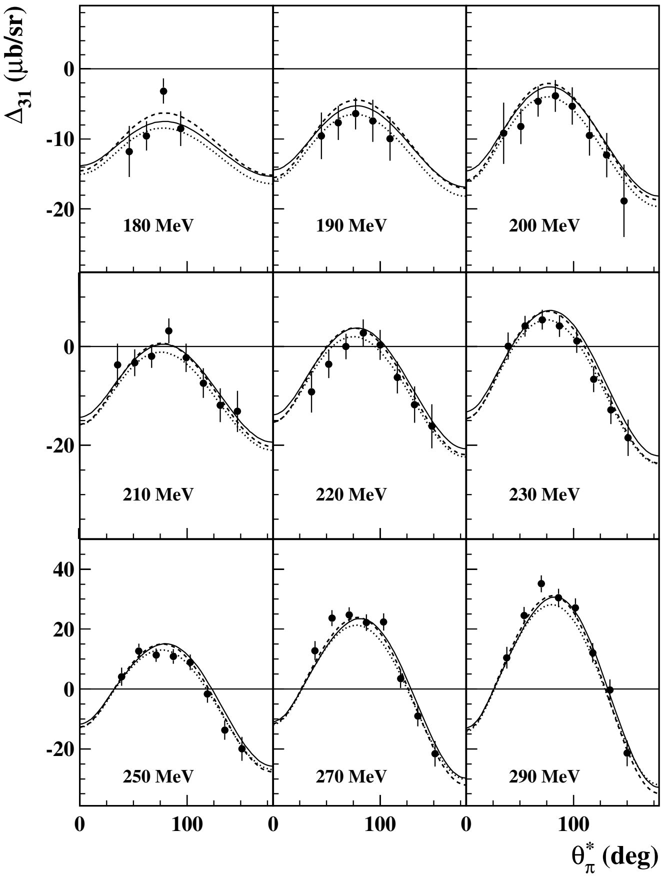

Fig. 7. The measured polarized differential cross-section $\Delta_{31} = (\mathrm{d}\sigma/\mathrm{d}\Omega)_{3/2} - (\mathrm{d}\sigma/\mathrm{d}\Omega)_{1/2}$ for the $\vec{\gamma}\vec{p} \to n\pi^+$ reaction for photon energies from 180 to 290 MeV (solid circles) is compared to the model predictions. Curves as in the previous figures. The errors shown are statistical only.

5 Partial-wave analysis

In the $\gamma N \to N\pi$ reactions, both incident particles and the final nucleon have two spin states yielding eight degrees of freedom altogether. Parity conservation reduces this number to a total of four complex amplitudes to describe the reaction. Allowing for one arbitrary phase factor, we therefore find seven independent physical quantities that need to be measured at any setting of E_γ and ϑ_π.

Using the Pauli amplitudes (F_1, F_2, F_3, F_4) introduced by Chew, Goldberger, Low and Nambu, the observables of the single-pion photoproduction can be expanded into a series of multipoles:

$$\mathcal{M}_{l\pm} = \{E_{l\pm}, M_{l\pm}\}$$

which conserve parity and total angular momentum J.

Here, E and M denote the electric or magnetic character of the incoming photon and the indices $l\pm$ describe the coupling of the pion angular momentum l and the nucleon spin to the total angular momentum $J = l \pm 1/2$. In general, these multipoles are complex functions of W, *i.e.* $\mathcal{M} = \mathcal{M}(W)$, where W is the total c.m.s. energy.

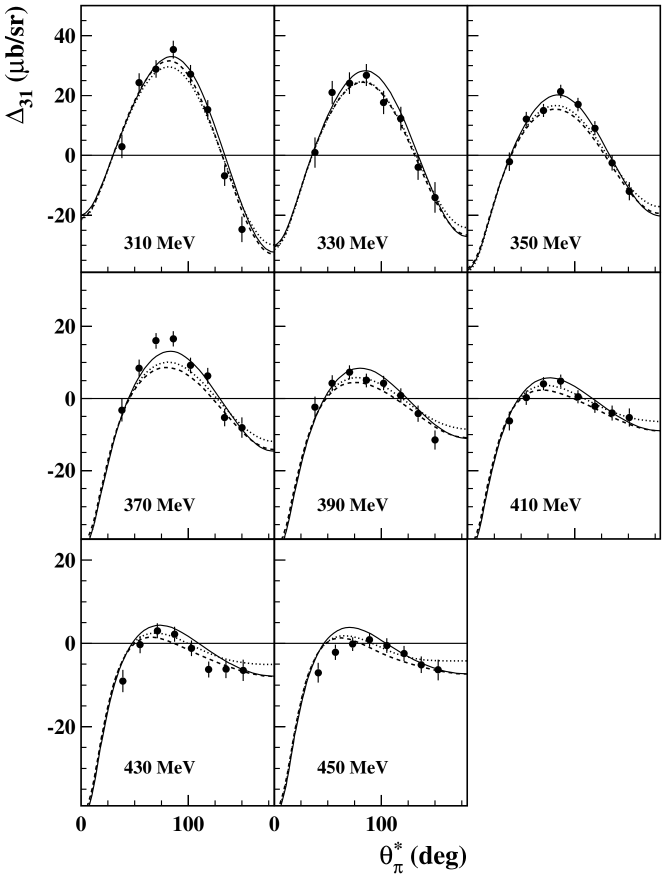

Fig. 8. As in fig. 7 but for photon energies from 310 to 450 MeV.

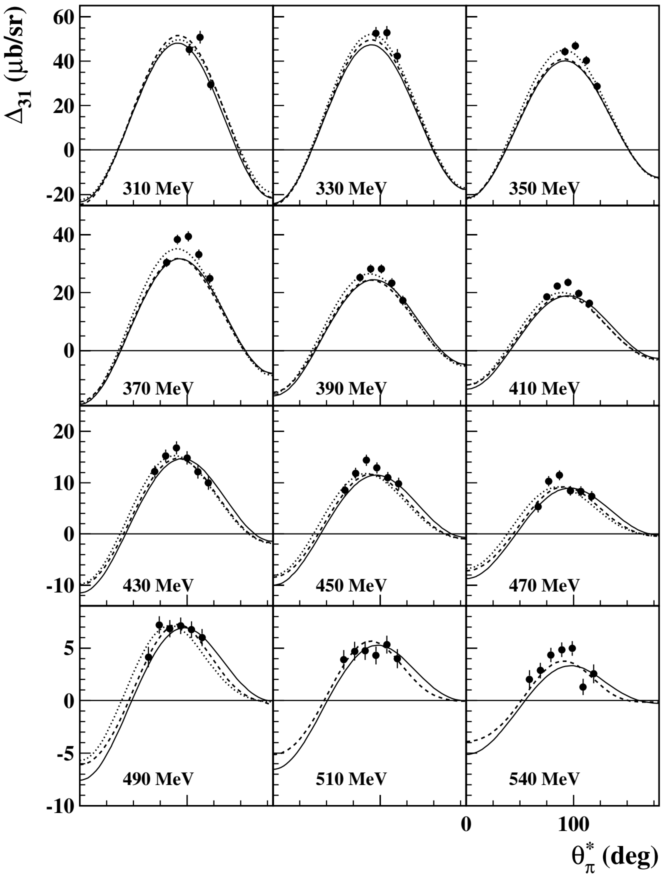

Fig. 9. The measured polarized differential cross-section Δ_{31} for the $\vec{\gamma}\vec{p} \to p\pi^0$ reaction for photon energies from 310 to 540 MeV. Curves as in figs. 3 and 4. The errors shown are statistical only.

As is well known, nine independent observables have to be measured to specify the multipole amplitudes to all orders in l_π. Such a complete database is not available at present. However, as shown in refs. [1,2], some constraints can be applied in order to perform an almost model-independent analysis with fewer observables.

In the energy range that we want to analyze, from 200 to 450 MeV, we consider only partial waves with $l_\pi \leq 1$ (s-p approximation) and then only the multipoles $E_{0+}, E_{1+}, M_{1-}, M_{1+}$ have to be taken into account. Due to the isospin dependence ($I = 1/2, 3/2$), 8 multipole amplitudes have to be determined:

$$E^{1/2}_{0+}, E^{3/2}_{0+}, E^{1/2}_{1+}, E^{3/2}_{1+}, M^{1/2}_{1-}, M^{3/2}_{1-}, M^{1/2}_{1+}, M^{3/2}_{1+}.$$

The contribution of higher partial waves ($l_\pi \geq 2$) was evaluated in the Born approximation [20] and added to the previous multipoles in the fitting procedure.

In the considered energy region, the real and imaginary parts of each multipole are related by the Fermi-Watson theorem

$$\mathcal{M}^I_{l\pm} = \left|\mathcal{M}^I_{l\pm}\right| e^{(i\delta^I_{l\pm} + n\pi)},$$

where $\delta^I_{l\pm}$ is the corresponding pion-nucleon scattering phase. As a consequence, 8 real quantities have to be determined. Strictly speaking, this theorem is valid only below the double-pion photoproduction threshold but it can be safely used below 450 MeV, since inelasticities are very small in that region.

The starting point of our analysis is the assumption, based on all existing multipole analyses, that, in the energy range considered, only the $E^{3/2}_{1+}$ and $M^{3/2}_{1+}$ multipoles show a resonant behavior and that all other multipoles have a smooth energy dependence. These nonresonating multipoles are then parameterized by a simple second-order polynomial function. The free variable x of the polynomial is taken as

$$x = q_\pi / m_\pi,$$

where q_π is the c.m.s. pion momentum, m_π the pion mass, and the polynomial is multiplied by the factor x^l in order to correctly reproduce the threshold behavior. Each multipole, apart from $E^{3/2}_{1+}$ and $M^{3/2}_{1+}$, is then written as

$$\mathcal{M}_{l\pm} \simeq \mathcal{M}^{NR}_{l\pm} = x^l \sum_{n=0}^{2} a_n x^n,$$

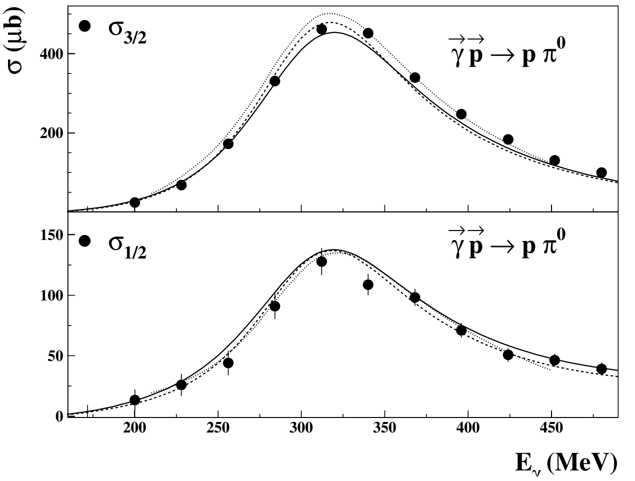

Fig. 10. The helicity-dependent cross-sections $\sigma_{3/2}$ and $\sigma_{1/2}$ for the $\vec{\gamma}\vec{p} \to p\pi^0$ reaction are compared to the model predictions. Continuous line: SAID; dashed line: MAID; dotted line: the multipole analysis presented in this work. Only statistical errors are shown.

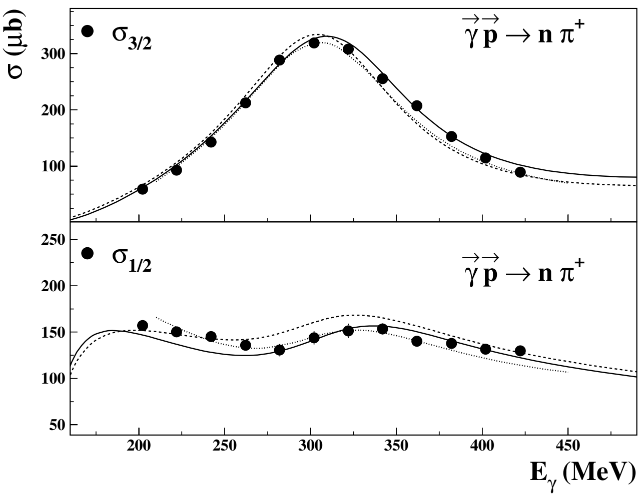

Fig. 11. As in fig. 10 but for the $\vec{\gamma}\vec{p} \to n\pi^+$ channel.

where the symbol $\mathcal{M}^{\mathrm{NR}}_{l\pm}$ denotes the nonresonant multipole component. The main advantage of such a parameterization is to take into account, although in a simple and phenomenological way, all possible nonresonant reaction mechanisms (Born terms, pion loops, etc.).

As stated before, this simple description is not suited for the $E^{3/2}_{1+}$ and $M^{3/2}_{1+}$ multipoles, which have a dominant resonant contribution due to the intermediate excitation of the $\Delta(1232)$-resonance. These two multipoles are then written as

$$\mathcal{M}_{l\pm} = \mathcal{M}^{\mathrm{NR}}_{l\pm} + \mathcal{M}^{\mathrm{R}}_{l\pm},$$

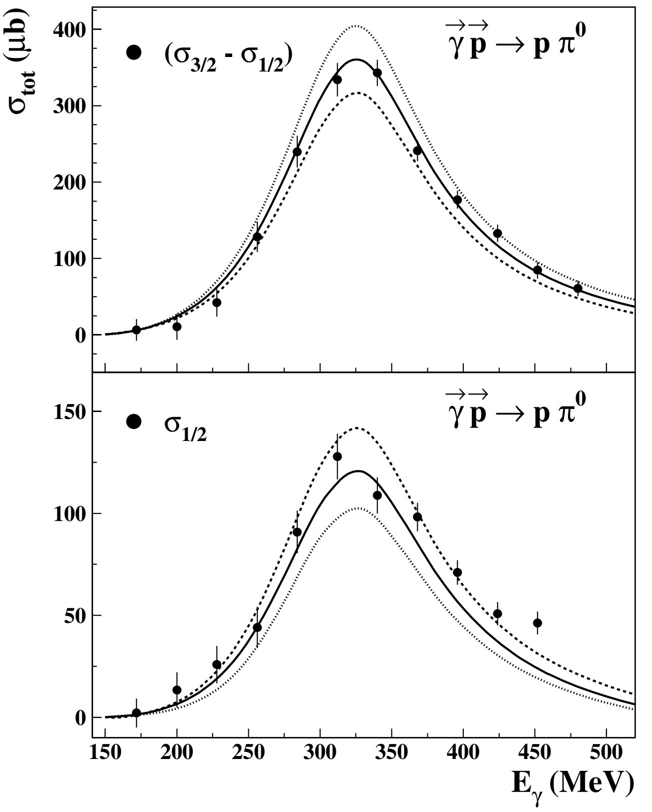

Fig. 12. The measured helicity-dependent cross-sections $\sigma_{31} = (\sigma_{3/2} - \sigma_{1/2})$ (top) and $\sigma_{1/2}$ (bottom) for the $\vec{\gamma}\vec{p} \to p\pi^0$ reaction are compared to the three different predictions of the HDT model: solid curve: $E2/M1 = -2.5\%$; dashed curve: $E2/M1 = 0$; dotted curve: $E2/M1 = -5.0\%$.

where, for the resonant contribution $\mathcal{M}^{\mathrm{R}}_{l\pm}$, following MAID [20], a Breit-Wigner energy dependence of the form

$$\mathcal{M}^{\mathrm{R}}_{l\pm}(W) = \overline{\mathcal{M}}_{l\pm} f_{\gamma N}(W) \times \frac{\Gamma_{\mathrm{tot}} W_R e^{i\phi_R}}{W_R^2 - W^2 - iW_R\Gamma_{\mathrm{tot}}} f_{\pi N}(W) C_{\pi N}$$

is assumed. The parameter $f_{\pi N}(W)$ is the usual Breit-Wigner factor describing the decay of a resonance R with total width Γ_R, spin j and energy W_R:

$$f_{\pi N}(W) = \left[\frac{1}{(2j+1)}\frac{1}{\pi}\frac{k_W}{|q_\pi|}\frac{m_N}{W}\frac{\Gamma_{\pi N}(W)}{\Gamma^2_{\mathrm{tot}}(W)}\right]^{1/2},$$

where k_W is the c.m.s. photon momentum at energy W. The factor $C_{\pi N}$ is $\sqrt{3/2}$ and $-1/\sqrt{3}$ for the $I = 3/2, 1/2$ multipoles, respectively. The factor $f_{\gamma N}$ parameterizes the W-dependence of the γNN^* vertex beyond the resonance peak, taking into account the corrections due to the interference with the nonresonant contribution:

$$f_{\gamma N}(W) = \left(\frac{k_W}{k_R}\right)^n \left(\frac{X^2 + k_R^2}{X^2 + k_W^2}\right), \quad n \geq l_\gamma,$$

where X is a damping parameter, assumed to be $X = 500$ MeV, and $k_R = k_W$ at $W = W_R$. The strength of the

Table 1. The database used in the present multipole analysis.

Reaction	Observable	E_γ range (MeV)	ϑ^*_π range (degrees)	Data set
$\gamma p \to p\pi^0$	$\mathrm{d}\sigma/\mathrm{d}\Omega$	[210,450]	[0,180]	[27]
$\vec{\gamma} p \to p\pi^0$	Σ	[210,430]	[0,180]	[27]
$\gamma \vec{p} \to p\pi^0$	T	[270,440]	[70,120]	[28]
$\gamma \vec{p} \to p\pi^0$	T	[280,450]	[70,120]	[29]
$\vec{\gamma} \vec{p} \to p\pi^0$	Δ_{31}	[330,450]	[70,120]	this work
$\gamma p \to n\pi^+$	$\mathrm{d}\sigma/\mathrm{d}\Omega$	[210,450]	[25,155]	this work
$\vec{\gamma} p \to n\pi^+$	Σ	[270,410]	[15,135]	[2]
$\gamma \vec{p} \to n\pi^+$	T	[220,425]	[35,135]	[30]
$\vec{\gamma} \vec{p} \to n\pi^+$	Δ_{31}	[210,450]	[25,155]	this work

transition is described by the amplitudes $\overline{\mathcal{M}}_{l\pm}$ that are considered as free parameters to be extracted from the analysis of the experimental data.

The unitary phase $\phi_R(W)$ is taken from the MAID analysis and adjusts the phase of the total multipole (nonresonant plus resonant term) to the corresponding pion-nucleon phase shift $\delta_{\pi N}$, in accordance with the Fermi-Watson theorem. The energy-dependent pion-nucleon scattering phases are taken from the SAID [19] analysis. In total 28 parameters have then to be determined in our fit.

In order to have a good sensitivity to as many as possible of the previous multipoles and to reduce the model dependence of this procedure, additional data were included in the fit. These were the $p\pi^0$ data from [27], which contain unpolarized differential cross-sections and the photon asymmetry Σ with full polar-angle coverage in the energy region with 210 MeV $< E_\gamma <$ 450 MeV, the Σ data for $n\pi^+$ in the photon energy range 270 MeV $< E_\gamma <$ 410 MeV from [2] and the target asymmetry data for both the $p\pi^0$ [28, 29] and $n\pi^+$ [30] channels. The database used for this purpose is summarized in table 1.

The so-called "energy-dependent" approach was used to extract the multipole amplitudes. The data at all energies were analyzed simultaneously in the fitting procedure. In this way continuity is built in from the beginning and the systematic errors of the experimental data tend to cancel out.

6 Results of the fit

The obtained results for the real parts of the multipoles are presented in fig. 13. Our results for the multipoles together with the corresponding fitting errors are shown as a dark band, while the different-style lines represent, as before, the predictions of the different models. As an example, the multipole fit results for the helicity-dependent total cross-sections $\sigma_{1/2}$ and $\sigma_{3/2}$ for the $N\pi$ channels are shown by the dotted lines in figs. 10 and 11. Taking into account only the experimental statistical errors, the overall reduced χ^2 of the fit is 1.17. Including systematic errors into the fit does not appreciably change the multipole behavior and decreases the χ^2 value only slightly.

Table 2. The Δ helicity amplitudes in ($10^{-3}\,\mathrm{GeV}^{-1/2}$) units.

	This work	MAID	SAID	PDG
$A_{1/2}$	-137 ± 5	-138	-129 ± 1	-135 ± 6
$A_{3/2}$	-256 ± 3	-246	-243 ± 1	-255 ± 8

In general, our empirical fit shows a good agreement with the existing multipole analyses; a few exceptions (as $E^{1/2}_{1+}$ and $M^{1/2}_{1+}$) could be due to the small sensitivity of our data set to these particular multipoles. However, it should be noted that these small multipoles are poorly known from the experimental point of view. The values for the Δ-resonance helicity amplitudes are given in table 2 in comparison to the SAID, MAID, and PDG [31] predictions. The error of our evaluation is only due to the fitting procedure and does not contain systematic effects. The resulting value of the $E2/M1$ ratio ($E2/M1 = -2.74 \pm 0.03$ %) is in good agreement with previous results [1,2].

The most realistic analysis on the $E2/M1$ ratio has been done by the BRAG Group [32] that performed different multipole analyses using a common database containing mainly the most recent measurements. From the combined set of fits this quantity was found to be $E2/M1 = -2.4 \pm 0.3\%$, where the error reflects the systematic uncertainty of the evaluation. This results from a 12% systematic uncertainty in the small electric multipole and only 1.6% in the dominant magnetic multipole. Therefore, also our evaluated helicity amplitudes $A_{1/2}$ and $A_{3/2}$ can be assumed to have a systematic uncertainty of only 1.6%. Much larger systematic deviations were observed for the nonresonant p-wave amplitudes, and this is also the case in our present analysis. In fig. 13 it can be seen that the resonant amplitudes of our new analysis and the previous analyses of HDT, SAID and MAID agree very well, but the nonresonant amplitudes show very significant deviations, especially for $E^{(1/2)}_{1+}$, $M^{(1/2)}_{1+}$ and $M^{(3/2)}_{1-}$. These amplitudes are completely determined by background contributions and are treated very differently in different approaches. Our fit comes close to the dispersion analysis of HDT, which is up to now the most reliable approach for the Δ region. Here our data can improve the existing partial-wave analyses. But, in order to get more reliable results on these nonresonant amplitudes, additional data is needed to resolve some of the ambiguities in the correlations of different multipoles. Such observables would be the target and recoil polarization and double-polarization observables with linearly polarized photons, which are proportional to products between real and imaginary parts of multipoles. By this way, the mainly real background amplitudes can be enhanced through interference with the $M1$ contribution of the Δ-resonance.

7 Conclusions

For the first time, a large set of high-quality double-polarization data for the $\gamma N \to N\pi$ channels has

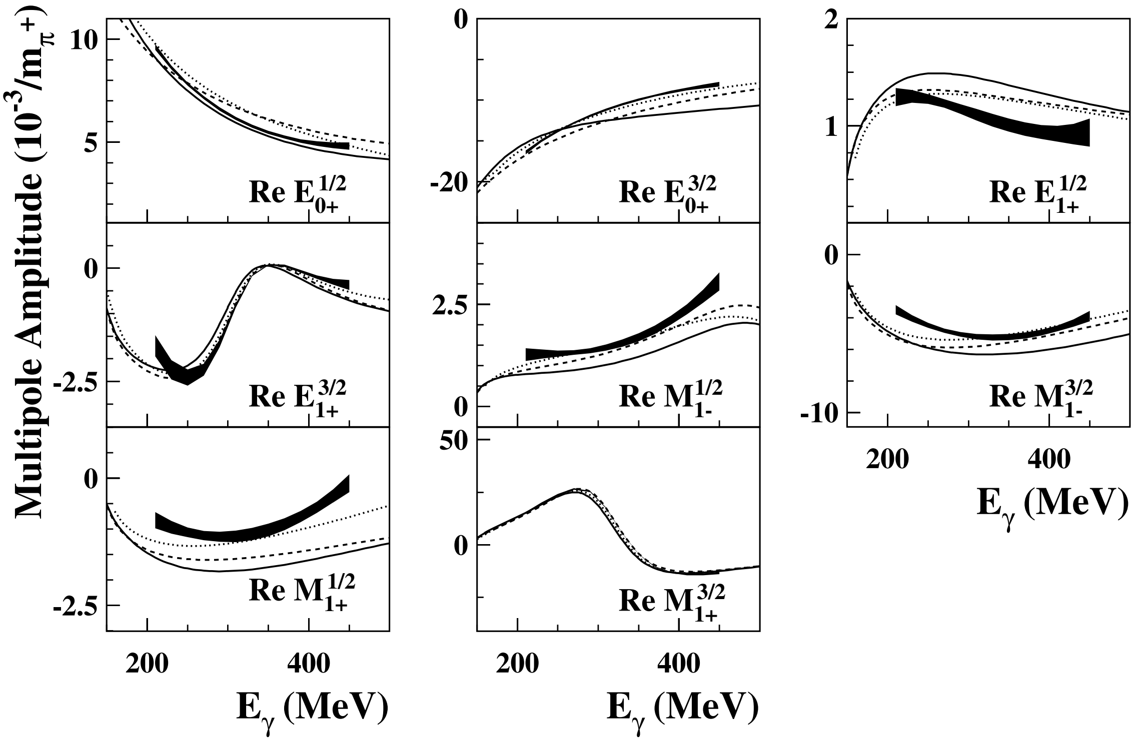

Fig. 13. The real parts of the fitted multipole amplitudes (dark bands) are compared to the model predictions. Continuous lines: SAID; dashed line: MAID; dotted line: HDT.

been obtained in the Δ-resonance region in the framework of the GDH experiment.

In order to see the impact of the new data on a partial-wave analysis and to compare the data with previous unpolarized and single-polarization data we have performed a multipole analysis. Guided by the phenomenological SAID analysis, we have used a quite general parameterization of the nonresonant background that allows the fit to go beyond Born terms and vector meson exchange. For the resonant multipoles we used the parameterization of MAID with only one free parameter for each multipole. In this way our analysis should be considered as an alternative, especially suited for high-precision data in the Δ region, where we can also focus on smaller background amplitudes. For the most important resonant $\Delta(1232)$ multipoles we find a very good agreement with previous analyses. The nonresonant background amplitudes, however, especially $E_{1+}^{(1/2)}, M_{1+}^{(1/2)}$ and $M_{1-}^{(3/2)}$, show significant deviations, which have to be investigated in future dedicated polarization experiments.

We gratefully acknowledge the help and hospitality of the MAMI staff for providing excellent beam conditions and support. This work was supported by the Deutsche Forschungsgemeinschaft (SFB 201, SFB 443, Schwerpunktprogramm 1034, and GRK683), the INFN (Italy), the FWO Vlaanderen (Belgium), the IWT (Belgium), the UK Engineering and Physical Science Council, the DAAD, JSPS Research Fellowship, and the Grant-in-Aid (Specially Promoted Research) in Monbusho, Japan.

References

1. R. Beck *et al.*, Phys. Rev. Lett. **78**, 78 (1997).
2. R. Beck *et al.*, Phys. Rev. C **61**, 035204 (2000).
3. G. Blanpied *et al.*, Phys. Rev. C **64**, 025203 (2001).
4. J. Ahrens *et al.*, Phys. Rev. Lett. **84**, 5950 (2000).
5. J. Ahrens *et al.*, Phys. Rev. Lett. **88**, 232002 (2002).
6. M. MacCormick *et al.*, Phys. Rev. C **55**, 41 (1996).
7. K. Aulenbacher *et al.*, Nucl. Instrum. Methods A **391**, 498 (1997).
8. I. Anthony *et al.*, Nucl. Instrum. Methods A **301**, 230 (1991); S. J. Hall *et al.*, Nucl. Instrum. Methods A **368**, 698 (1996).
9. I. Preobajenski, PhD Thesis, University of Mainz, 2001.
10. C. Bradtke *et al.*, Nucl. Instrum. Methods A **436**, 430 (1999).
11. G. Audit *et. al.*, Nucl. Instrum. Methods A **301**, 473 (1991).
12. S. Altieri *et al.*, Nucl. Instrum. Methods A **452**, 185 (2000).
13. M. Sauer *et al.*, Nucl. Instrum. Methods A **378**, 146 (1996).
14. A. Braghieri *et al.*, Nucl. Instrum. Methods A **343**, 623 (1994); W. Langgärtner *et al.*, Phys. Rev. Lett. **87**, 052001 (2001).
15. R. Crawford *et al.*, Nucl. Phys. A **603**, 303 (1996).
16. J. Ahrens *et al.*, Phys. Lett. B **551**, 49 (2003).
17. A. Braghieri *et al.*, Phys. Lett. B **363**, 46 (1995).
18. O. Hanstein *et al.*, Nucl. Phys. A **632**, 561 (1998).
19. R.A. Arndt *et al.*, Phys. Rev. C **66**, 055213 (2002); solution SM02K.
20. D. Drechsel *et al.*, Nucl. Phys. A **570**, 580 (1999); solution MAID2000.

21. K.G. Fissum *et al.*, Phys. Rev. C **53**, 1278 (1996)
22. G. Fischer *et al.*, Nucl. Phys. B **16**, 93 (1970); Z. Phys. **253**, 38 (1972).
23. K. Büchler *et al.*, Nucl. Phys. A **570**, 580 (1994).
24. H.W. Dannhausen *et al.*, Eur. Phys. J. A **11**, 441 (2001).
25. B. Krusche *et al.*, Eur. Phys. J. A **9**, 309 (1999).
26. H. Genzel *et al.*, Z. Phys. **268**, 43 (1974).
27. R. Leukel, PhD Thesis, University of Mainz, 2001.
28. A. Bock *et al.*, Phys. Rev. Lett. **81**, 534 (1998).
29. A.A. Belayev *et al.*, Nucl. Phys. B **213**, 201 (1983).
30. H. Dutz *et al.*, Nucl. Phys. A **601**, 319 (1996).
31. Particle Data Group (K. Hagiwara *et al.*), Phys. Rev. D **66**, 010001 (2002).
32. BRAG Group (R.A. Arndt *et al.*), nucl-th/0106059.